Title

First Results From the Retrieved Column O/N2 Ratio From the Ionospheric Connection Explorer (ICON): Evidence of the Impacts of Nonmigrating Tides

Journal

Journal of Geophysical Research Space Physics, 126(9)

ISSN

2169-9380

Authors

England, Scott L
Meier, RR
Frey, Harald U
et al.

Publication Date

2021-09-01

DOI

10.1029/2021ja029575

Peer reviewed

Published in final edited form as:
J Geophys Res Space Phys. 2021 September ; 126(9): . doi:10.1029/2021ja029575.

First results from the retrieved column O/N_2 ratio from the Ionospheric Connection Explorer (ICON): Evidence of the impacts of nonmigrating tides

Scott L. England[1], **R. R. Meier**[2,3], **Harald U. Frey**[4], **Stephen B. Mende**[4], **Andrew W. Stephan**[5], **Christopher S. Krier**[1], **Chihoko Y. Cullens**[4], **Yen-Jung J. Wu**[4], **Colin C. Triplett**[4], **Martin M. Sirk**[4], **Eric J. Korpela**[4], **Brian J. Harding**[4], **Christoph R. Englert**[5], **Thomas J. Immel**[4]

[1]Aerospace and Ocean Engineering, Virginia Polytechnic Institute and State University, Blacksburg, United States

[2]Department of Physics and Astronomy, George Mason University, Fairfax, United States

[3]U.S. Naval Research Laboratory, Emeritus, Washington DC, United States

[4]Space Sciences Laboratory, University of California Berkeley, Berkeley, United States

[5]U.S. Naval Research Laboratory, Washington DC, United States

Abstract

In near-Earth space, variations in thermospheric composition have important implications for thermosphere-ionosphere coupling. The ratio of O to N_2 is often measured using far-UV airglow observations. Taking such airglow observations from space, looking below the Earth's limb allows for the total column of O and N_2 in the ionosphere to be determined. While these observations have enabled many previous studies, determining the impact of non-migrating tides on thermospheric composition has proved difficult, owing to a small contamination of the signal by recombination of ionospheric O^+. New ICON observations of far UV are presented here, and their general characteristics are shown. Using these, along with other observations and a global circulation model we show that during the morning hours and at latitudes away from the peak of the equatorial ionospheric anomaly, the impact of non-migrating tides on thermospheric composition can be observed. During March – April 2020, the column O/N_2 ratio was seen to vary by 3 – 4 % of the zonal mean. By comparing the amplitude of the variation observed with that in the model, both the utility of these observations and a pathway to enable future studies is shown.

Plain Language Summary

At high altitude in the atmosphere, mixing of the gas via turbulence becomes less important, and mix of atmospheric species begins to vary with altitude, depending on the mass of the atom or molecule. At these altitudes, the composition of the atmosphere can vary greatly with location and time in a manner not seen in the lower levels of the atmosphere. This same high-altitude region overlaps with the charged particle environment known as the Earth's ionosphere. How the atmosphere and ionosphere interact is in-part determined by the composition of the atmosphere.

Corresponding author: Scott L. England (englands@vt.edu).

Measuring this composition is therefore important and is done regularly using observations in the far ultraviolet. These reveal much of the compositional variation, but a small contaminating signal from the ionosphere has made detecting some small changes produced by waves in the atmosphere a challenge. Here, new observations in the far UV are introduced and their general properties shown. By selecting a specific location and time and utilizing supporting data and a global model we are able to show the change in the composition produced by a certain class of wave in the atmosphere. This demonstrates the utility of these new observations and provides a pathway to futures studies.

1. Introduction

The ratio of atomic oxygen to molecular nitrogen concentrations in the thermosphere has important consequences for chemical processes in both the atmosphere and the ionosphere. O and N_2 are the dominant species in the middle and upper thermosphere (e.g., Hedin et al., 1977). The density of O affects the production rate of O^+ in the F-region ionosphere (primarily via charge exchange with N_2^+, with a contribution from direct ionization of O; e.g. Torr and Torr, 1985). The lifetime of O^+ at F-region altitudes is governed by dissociative recombination with N_2 (e.g., Schunk, 1983). Thus, measuring the ratio of O to N_2 provides essential knowledge of the ionospheric state. An effective technique for determination of the thermospheric O/N_2 ratio exists in simultaneous observation of photoelectron generated far ultraviolet (FUV) airglow from O (the 135.6 nm doublet) and N_2 (the Lyman-Birge-Hopfield, LBH band). Strickland et al., [1995] demonstrated that earth nadir and sub-limb observations of these airglow emissions can be used to determine the thermospheric column O/N_2 ratio ($\Sigma O/N_2$). Using such sub-limb observations of the emission rate ratio yields a ratio of O/N_2 column density of these two species from below the observer down to an altitude corresponding to an N_2 column density of 10^{17} cm^{-2}, which is typically an altitude corresponding to 130 – 140 km altitude range in thermospheric models. Such sub-limb FUV observations have been used to provide observations of $\Sigma O/N_2$ from a wide variety of satellite datasets including Polar Bear (Evans et al., 1995), Dynamics Explorer 1 (Nicholas et al., 1997; Strickland et al., 1999), the Thermosphere, Ionosphere, Mesosphere Energetics and Dynamics Global Ultraviolet Imager (TIMED-GUVI; e.g., Zhang et al., 2004) and Global-scale Observations of the Limb and Disk (GOLD; e.g., Oberheide et al., 2020).

One of the many applications of the $\Sigma O/N_2$ measurement is to investigate composition changes associated with atmospheric tides. Non-migrating tides produce clear zonal variations in the thermospheric winds and temperatures at fixed local times, and are a source of significant longitudinal variation in the low-latitude ionosphere (e.g., Sagawa et al., 2005, Immel et al., 2006, Goncharenko et al., 2010). While it is generally considered that modulation of the E-region dynamo by tidal winds is the primary mechanism through which non-migrating tides impact the longitudinal structure of the ionosphere, perturbations to photochemical equilibrium arising from tidal modulation of the $\Sigma O/N_2$ have also been proposed (e.g., England et al., 2010, Zhang et al., 2010).

Atmospheric tides can perturb the ratio of O and N_2 at altitudes above the homopause as a result of the unequal impact of the vertical tidal winds on species with different

scale heights. This can be illustrated using the continuity equation for linear, plane-wave perturbations in the absence of rapid diffusion:

$$\frac{\widetilde{\rho_i}}{\overline{\rho_i}} \propto \frac{1}{\omega}\left(\frac{\widetilde{w}}{H_i} - \nabla \cdot \widetilde{V}\right), \quad (1)$$

where $\tilde{\rho}_i/\bar{\rho}_i$ is the density perturbation relative to the mean value for a given species, ω is the wave frequency, $\widetilde{w}$ is the vertical velocity perturbation, H_i is the species-dependent scale height and $\widetilde{V}$ is the velocity perturbation (e.g., Dudis and Reber, 1976; Cui et al., 2014). From Equation 1, it is apparent that the horizontal winds associated with an atmospheric tide modify the density of all species equally, whereas the impact of the vertical wind is inversely proportional to the species scale height. At Mars, where atmospheric tides are particularly large in amplitude, mass spectrometer data have demonstrated a clear inverse scale-height relationship to the tidal perturbations seen in numerous atmospheric species (England et al., 2016). At Earth, tidal-induced variations in the density of minor species such as NO have been observed (e.g., Oberheide and Forbes, 2008). The identification of non-migrating tides in FUV sub-limb observations of $\Sigma O/N_2$ has been attempted, where Zhang et al., [2010] reported a moderate variation in the $\Sigma O/N_2$ ratio with longitude that appeared to match the patterns expected from the diurnal eastward wavenumber 2 (DE2) and 3 tides (DE3). However, further analysis by Kil and Paxton, [2011] suggested that the origin of this signature was not variation in $\Sigma O/N_2$, but rather a tidal variation in O^+ at high altitude (well above the photoelectron produced O airglow) that was misinterpreted as a variation in O/N_2. This result was further confirmed by Stephan et al., [2019] using data in both the FUV and Extreme UV from the LITES instrument on the International Space Station. Such a misinterpretation is possible as O^+ radiative recombination can yield the same 135.6 nm doublet as photoelectron excitation of O, so while the latter is dominant during the daytime, presence of the former can lead to a small degree of error in the determination of daytime $\Sigma O/N_2$. Kil et al., [2013] further quantified the impact of O^+ radiative recombination on $\Sigma O/N_2$ determined from TIMED-GUVI observations and showed this was of 5 – 10 % for data around 15:00 local time (LT) during August – September 2002, at low geomagnetic activity. This is clearly important in the case of identifying the impact of non-migrating tides on $\Sigma O/N_2$, as these produce only a small variation in the composition (~5 % of the zonal mean).

This study has three purposes. The first is to present new $\Sigma O/N_2$ observations from ICON FUV. The general characteristics of these, their variation with solar zenith angle, latitude and season is presented in Section 3. The second is to use these data, along with other observation from ICON and the TIEGCM model to demonstrate that in limited circumstances the impact of non-migrating tides on $\Sigma O/N_2$ can be found using sub-limb FUV observations (Section 4). The third is to determine both the magnitude of the O/N_2 variations produced by non-migrating tides and to identify times when the retrieved $\Sigma O/N_2$ may be impacted by O^+ radiative recombination to a degree that renders this technique unreliable to identify any tidal signatures in $\Sigma O/N_2$ (Section 4).

2. Data

This section describes the ICON observational data used in this study, including $\Sigma O/N_2$, O^+ profiles and NmF2, horizontal winds, neutral temperatures, and 557.7 nm airglow volume emission rate. A description of the TIEGCM model, which uses tides derived from the ICON observations as part of its lower boundary condition is also given.

2.1 Far UV Brightness and $\Sigma O/N_2$

The ICON Far Ultra-Violet Imager (ICON-FUV; Mende et al., 2017) is a spectrographic imager that observes airglow emissions from the Earth's limb and sub-limb simultaneously. Observations are made in two spectral passbands: Short wave (SW) centered on the 135.6 nm OI doublet, and long wave (LW) capturing a portion of the Lyman-Birge-Hopfield (LBH) N_2 bands centered on 157 nm. The thermospheric $\Sigma O/N_2$ is found by using the brightness observed in these two passbands for the data taken during the daytime below the limb of the Earth, such that the entire vertical column of O and N_2 is captured (Meier, 2021; Stephan et al., 2018). For ICON-FUV, the observed sub-limb airglow comes from approximately 7.5° great circle away from the spacecraft, and represents a slant integral, rather than purely vertical. Thus, these data represent an average over some small horizontal range. Here we use version 04 of the derived $\Sigma O/N_2$ product (open access described in the acknowledgements section). Section 3 presents an analysis of 6 months of these observations, describing their general properties. Section 4 uses these data to investigate atmospheric tides and highlight their utility and current limitations.

2.2 Extreme UV observations and O^+ altitude profiles

The ICON Extreme Ultraviolet Spectrograph (ICON-EUV; Sirk et al., 2017) is an imaging spectrometer that observes airglow emissions from the Earth's limb in a spectral range from 54 – 88 nm. The altitude profile of O^+ is estimated using daytime observations of the 61.7 nm O^+ triplet and the 83.4 nm O^+ triplet (Stephan et al., 2017). Here we use version 03 of the derived O^+ density profiles and corresponding ionospheric NmF2 values. These data are used in Section 4 to identify the signature of atmospheric tides in the ionospheric O^+.

2.3 Horizontal vector winds and 557.7 nm airglow

The ICON Michelson Interferometer for Global High-Resolution Thermospheric Imaging (ICON-MIGHTI; Englert et al., 2017) is a Doppler Asymmetric Spatial Heterodyne (DASH) spectrometer that observe airglow emissions from the Earth's limb in the visible and near infrared range. Observations of the visible emission from atomic oxygen at 630.0 nm and 557.7 nm are used to determine line-of-sight Doppler shifts. By employing two orthogonal line of sight measurements of the limb, the horizontal wind velocity is retrieved at altitudes between 90 and 300 km (Harding et al., 2017). Here we use version 04 of the derived horizontal vector winds and relative volume emission rate of the 557.7 nm emission. These data are used in Section 4 to both identify the atmospheric tides present in the lower and middle thermosphere and provide a lower boundary condition to the TIEGCM model.

2.4 O_2 Atmospheric band temperatures

ICON-MIGHTI observations of the near infrared O_2 Atmospheric band around 762 nm are used to determine the lower thermospheric temperature (Stevens et al., 2018). Here we use version 04 of the derived atmospheric temperatures. These data are used in Section 4 to both identify the atmospheric tides present in the lower thermosphere and provide a lower boundary condition to the TIEGCM model.

2.5 TIEGCM simulated $\Sigma O/N_2$

For comparison with and interpretation of ICON measurements in Section 4, $\Sigma O/N_2$ are also computed from the Thermosphere-Ionosphere-Electrodynamics General Circulation Model for the Ionospheric Connection Explorer (TIEGCM-ICON; Maute, 2017). This version of the TIEGCM V2.0 model (see http://www.hao.ucar.edu/modeling/tgcm/tiegcm2.0) uses atmospheric tides derived from the ICON-MIGHTI wind and temperature data to perturb its lower boundary (at ~97 km altitude) for simulation of the thermospheric and ionospheric conditions that best correspond to those present during the ICON mission. Specifically the wind and temperature observations from ICON in the 90 – 103 km altitude range are used to determine the global tidal spectrum using the Hough Mode Extension (HME) technique (Forbes et al., 2017, Cullens et al., 2020). This is necessary as the TIEGCM model requires a self-consistent lower boundary to be specified across the entire globe, whereas the ICON observations at this altitude only cover a limited latitude range (10° south – 40° north). As such, there are some limitations to this approach that are worth mentioning in the context of the present study. First is that Forbes et al., [2017] noted that the limited latitudinal range covered by ICON can lead to aliasing of some tidal components, including DE3. The second limitation is that when the spacecraft is in the South Atlantic Anomaly (SAA), the wind and temperature observations are compromised, effectively reducing the sampling on the limb in the region below the equator in the South America / Atlantic region. The impact of this was examined pre-flight by Cullens et al., [2020]. Using in-flight data, the DE3 structure revealed with the ICON HME version 01 have been compared to both the original ICON observations and the Climatological Tidal Model of the Thermosphere (Oberheide et al., 2011). A full comparison of these is beyond the scope of this study but we will note here that in general the climatological results from these three agree well, suggesting that at least over longer time periods the impact of data missing near the SAA is minimal. However, given these potential imitations of the lower boundary forcing in TIEGCM, the results shown in Section 4 will be discussed in this context.

3. An examination of the retrieved $\Sigma O/N_2$

This section will present the observed properties of the FUV brightness and retrieved $\Sigma O/N_2$ ratios. Using the first 6 months of 2020 as an example, the key properties will be highlighted, along with some seasonal trends.

3.1 Observed FUV brightness

Insight into the ICON FUV dataset can be gained by examining the brightness observed in the SW and LW channels over a range of conditions. Figure 1 shows the observed brightness in both channels for one day of observations (March 15th, 2020 is shown here

as an example from approximately the middle of the 6-month dataset that will be examined here). The location of the observations for this day are shown in terms of latitude, LT and solar zenith angle (SZA) of the intersection of the instrument's line of sight with a surface at 150 km altitude above the geoid (corresponding to the location of the $\Sigma O/N_2$ measurement). For this day, the daytime data are all located within the northern hemisphere, but this varies with orbital precession. Each of the observations shown represents a measurement from a 12 second exposure. As expected, both the SW and LW channels show a strong variation in brightness with SZA as this is the primary factor in determining the total rate of photoelectron production, which is the dominant excitation process for the emission seen at these wavelengths. This correlation is clear in Figure 1, as is the related local time influence on the brightness observed. Very little scatter beyond these geometric trends is seen. The relative brightness between the two channels is reflective of the passbands and the relative brightness of the oxygen and nitrogen-related dayglow (see Mende et al., 2017).

Figure 2 shows the observed brightness over a 45-day period, which allows ICON to sample a full range of latitudes and local times due to orbital precession. Here the first 45 days of 2020 are shown, corresponding to nearby solstice conditions with an associated strong latitudinal asymmetry in SZA (not shown). SZA dependence of the brightness of both the SW and LW channel data is evident, with the brightest emissions seen near the subsolar point (close to noon in the southern hemisphere) and the dimmest emissions seen near the terminators.

Taking the ratio of the SW to LW brightness (Figure 2c) eliminates some of the strong SZA dependence and allows for a first-order view of the impacts of varying $\Sigma O/N_2$ on the emissions. Plotting this ratio for all the points in the 45-day period reveals two overlapping patterns. First is the strong gradient in latitude, with the highest SW/LW ratios tending to be seen at higher northern latitudes. The second is a change with season as the later days within this range show generally higher SW/LW ratios at all latitudes (seen in the orange colors appearing diagonally from the northern higher latitudes at early LT to southern latitudes at later LT). Both of these patterns can be understood in terms of the expected seasonal variation in $\Sigma O/N_2$, with lower $\Sigma O/N_2$ expected in the summer hemisphere near solstice and generally higher $\Sigma O/N_2$ expected across this region nearer equinox (see Jones Jr et al., 2018 and references therein). The variation in the $\Sigma O/N_2$, derived using these data, is examined in the following section.

3.2 Observed $\Sigma O/N_2$

Figure 3 shows the retrieved $\Sigma O/N_2$ for January 2nd, 2020. For this example, the observations cover two portions of the latitude – SZA parameter space such that one covers all dayside SZA at a near constant latitude in the southern hemisphere and the other spans latitude with increasing SZA. This yields two examples of the variations expected in $\Sigma O/N_2$, if these were the dominant controlling factors. This is revealed by a comparison to NRLMSISE-00 (Picone et al., 2002; MSIS hereafter). While a newer version of the MSIS model exists (Emmert et al., 2020), the earlier version is used here to allow for a comparison to published results from TIMED-GUVI, described below. The predicted $\Sigma O/N_2$ from MSIS show two clear patterns with SZA, corresponding to the two regions of observation. The

ICON values reveal some evidence of this bifurcated pattern but with a much smaller difference between the two regions and also clear geophysical variability about this trend. Further, the $\Sigma O/N_2$ values retrieved from ICON observations are lower than MSIS for almost all cases. These two observations are worth considering in more detail. First, the variation in the retrieved values is compared to the uncertainty determined for each value, shown in panel c of Figure 3. The uncertainties clearly increase slightly with increasing SZA. This may be expected as the photoelectron production peak rises in altitude with increasing SZA and thus the $\Sigma O/N_2$ is less sensitive to N_2 at lower altitudes, thereby increasing the uncertainty in the $\Sigma O/N_2$. At lower SZA, the uncertainties are well within ~5 – 10% of the retrieved value, and smaller than the spread seen in Figure 3b, suggesting that significant geophysical variability is present on this day. Second, the systematic difference with MSIS is examined using a larger data sample, to avoid any issues with conditions on a single day. Using 180 days, the ratio of the retrieved $\Sigma O/N_2$ from ICON is compared to that predicted with MSIS, and shown vs LT in Figure 3d. While significant spread in these values is seen, the mean at each LT is relatively constant and below 1 for each one-hour LT bin. Further, it is worth noting that a large portion of the spread that is visible comes from the points below the 5^{th} and above the 95^{th} percentile (see orange lines in Figure 3d). Taking an average over all LT, the mean value of the ICON/MSIS ratio is 0.84, with a standard deviation of 0.089 (approximately 10%). Meier et al. [2015] reported a similar offset when comparing TIMED-GUVI $\Sigma O/N_2$ values to MSIS. Considering only the values from 2007 (near solar minimum), Meier et al. [2015] reported a ratio of 0.89 (see their Figure 20). Given that the ICON and GUVI datasets do not span the same time or latitude range, the overall agreement in these values is within the uncertainties of the two datasets and suggests that the ICON $\Sigma O/N_2$ values (which come from sub-limb observations) are in family with those reported by Meier et al., [2015] using the GUVI limb observations.

Figure 4 shows the effect of seasonal changes on the $\Sigma O/N_2$ retrieved from ICON and predicted from MSIS. Here only values near to local noon (11 – 13 hours LT) are shown as this both eliminates any LT variation that may confuse the seasonal changes and limits the data to the region with the lowest measurement uncertainty. Each panel represents the data from a 45-day period, in which panels a and b correspond to days 1 – 45 (post northern winter solstice; matching Figure 2), panels c and d correspond to days 46 – 90 (approaching equinox) and panels e and f correspond to days 136 – 180 (approaching northern summer solstice). For days 1 – 45, a strong gradient with latitude is seen, as expected from Figure 2 and consistent with the seasonal variations reported in O/N_2 (e.g., Jones Jr et al., 2018). Following this semi-annual and annual pattern, the values close to solstice are generally higher at all latitudes and the latitudinal gradient is essentially reversed by days 136 – 180. All seasonal changes are seen in the MSIS values, indicating that the seasonal trends in ICON retrieved $\Sigma O/N_2$ values vary are in agreement with previous observations.

4. The signature of nonmigrating atmospheric tides in the $\Sigma O/N_2$

Using the $\Sigma O/N_2$ values retrieved from ICON, we can examine the signature of non-migrating tides on the composition of the middle thermosphere. The first step is to select a time period when non-migrating tides are seen clearly, such that their signature can be identified. This is accomplished with a tidal analysis of the MIGHTI horizontal wind

and temperature data (similar to the proof of concept presented by Cullens et al., 2020, which used TIME-GCM model output as a proxy for ICON observations). Figure 5 shows the amplitude of the diurnal eastward wavenumber 3 (DE3) and semi-diurnal eastward wavenumber 2 (SE2) tides as functions of latitude and day of year for the first 100 days of 2020 at 97 km altitude (where temperature and horizontal wind data are available through at all local times). The DE3 is known to have a peak in amplitude around February – March during most years (e.g., Oberheide and Forbes, 2008). Indeed, a peak is seen in Figure 5e around days 30 – 90 in the meridional winds near the equator and in Figure 5c, around days 60 – 100 in the zonal winds north of the equator. SE2 is the second strongest non-migrating tide during this time period that also produces a wavenumber-4 signature in a fixed LT frame The diurnal westward 5, semi-diurnal westward 6, terdiurnal eastward 1 tides can also produce wavenumber-4 signatures (e.g. Forbes et al., 2006). An examination of the amplitudes of these other tides observed by ICON during this time period revealed them to be negligible. This is seen to be weaker than DE3 throughout this time period, but is still present with some measurable amplitude, especially in the meridional winds around days 60 – 100.

Comparing the latitudinal structure of the DE3 temperatures and winds to those derived from TIMED observations (Oberheide and Forbes, 2008) reveals some differences that are worth noting. The meridional winds shown in Figure 5 appear to be symmetric about the equator, which is broadly consistent with the TIMED observations shown in Oberheide and Forbes, [2008]. However, the TIMED observations show an antisymmetric pattern in the temperature and zonal winds. In the DOY 60 – 100 range, the zonal winds in Figure 5 show an approximately antisymmetric pattern, but the latitudinal structure of the temperatures do not match these. This may be a result of the aliasing described in Section 2.5. As this pattern does not quite match that used in the HME fitting, this may have some impact on how well the TIEGCM model can reproduce the observed winds at higher altitudes (see Figure 8 and related discussion).

Figure 5 shows the tides determined at the base of the thermosphere, where the temperature and wind fields are available at all LT (which are required to provide the lower boundary forcing for the TIEGCM model). With the knowledge that the dominant non-migrating tides are associated with eastward moving wavenumber-4 signatures in a fixed LT frame, we can examine corresponding wavenumber-4 signatures in the winds near the photoelectron production peak. In the case of ICON-MIGHTI observations, daytime observations are consistently available near 150 km using the 557.7 nm observations. Using daytime only observations, it is not possible to identify the full tidal spectrum, but the variation in phase of any tidal signature with LT can help to identify which tides may be present at this altitude. Figure 6 shows the wavenumber-4 component of the averaged meridional and zonal winds between 150 km and 160 km altitude, averaged over days 75 – 100 (when DE3 is seen to be strongest). This figure uses data from 25 – 35° north, to correspond to the $\Sigma O/N_2$ values examined below. It is worth noting here that in the 150 – 160 km altitude range that is used in Figure 6, the average uncertainty per sample is 7 m/s. For either the ascending or descending node, an average of 450 data points per day are used in the fit, yielding an uncertainty in the wavenumber-4 fit of around 0.6 m/s. A clear eastward moving signature is seen in both the zonal and meridional winds and is clearest in the zonal winds. This may

be expected as the symmetric component of DE3 becomes dominant over the antisymmetric component with increasing altitude in the thermosphere, and is primarily characterized by zonal winds, rather than meridional winds (e.g. Oberheide and Forbes, 2008). The best fit phase shift in the zonal wind and meridional wind (shown with the dotted black line) is 5.12° / hour and 7.00° / hour, respectively. The phase shifts of the zonal wind and meridional wind fall between that expected for DE3 (3.75° / hour such that it moves 90 degrees in 24 hours) and SE2 (7.5° / hour such that it moves 90 degrees in 12 hours) and is consistent with a mixture of these two waves being present, as indicated from the lower-altitude data (Figure 5).

From the phase progression in a fixed local time frame described above, the eastward moving non-migrating tides seen in Figure 5 and Figure 6 are expected to produce a wavenumber-4 signature in the $\Sigma O/N_2$ when viewed in a fixed LT frame. Figure 7 shows the wavenumber-4 component of the $\Sigma O/N_2$ retrieved from ICON as functions of LT and day of year (DOY). Note that the LT sampled at any given latitude decreases with increasing day of year due to orbit precession. Data are shown at 25 – 35° north, where the DE3 is still seen clearly in MIGHTI data and the impact of any O^+ radiative recombination is lower than near to the equator, as a result of the lower O^+ density observed. The wavenumber-4 fit is performed for each day, and these are shown with both the corresponding LT and day of year. As the observations at this latitude range on a single day are sampled at two LT, the data are split into ascending and descending portions of the orbit. The ascending portion samples this latitude range during daytime from DOY 64 – 81, whereas the descending portion covers DOY 75 – 93. Figure 5 suggests that the DE3 tide is strongest between DOY 75 – 93 of this range but is clearly present throughout this entire range. The ascending portion sees a clear wavenumber-4 structure in the $\Sigma O/N_2$ between DOY 75 – 81, corresponding only to LT before 11 hours. With just ~3 hours of LT covered, no clear phase progression is evident. After ~11 LT (before DOY 75), the signal is less clear, which could be evidence of O^+ radiative recombination, a weaker tidal signature at this DOY range, or a change in the tidal signature with LT. Examining the data from the descending portion of the orbit, a clear wavenumber-4 signature is seen moving eastwards with LT between DOY 82 – 93 (corresponding to LT 7.4 – 12.9 hours). With ~5.5 hours of LT, the phase speed can be estimated, and appears to match that of DE3 (shown by the black line). The amplitude seen during this DOY range is ~3 – 4 % of the zonal mean value. It is worth noting here that in the 7 – 16 LT range that is used in Figure 7, the average uncertainty per sample is 7.3%. For either the ascending or descending node, an average of 810 data points per day are used in the fit, yielding an uncertainty in the wavenumber-4 fit of around 0.5 %. As with the data from the ascending portion of the orbit, the data at later LT show a less clear signature. However, for the descending portions these cover DOY 75 – 82, when the ascending portion still sees a strong signature, ruling out a weaker tidal signature at these DOY as the origin of this. This leaves the change in tidal signature with LT and a contribution of O^+ radiative recombination as possibilities for the change in characteristic of the wavenumber-4 pattern seen at later LT.

One feature that is evident, but as of yet unexplained is the similarity in the longitude of the maximum seen in the ascending and descending data in the DOY 75 – 82 range. Given the

~4 hour LT difference between these two samples, for a DE3 tide, a difference in longitude of 60 degrees may be expected, but this is not apparent in this date range.

Using the tides identified in the upper mesosphere and lower thermosphere region (Figure 5 and similar) and the HME fits to these (Forbes et al., 2017) it is possible to perturb the lower boundary of the TIEGCM model (near 97 km altitude) such that it reproduces the tides observed by ICON (Maute et al., 2017) to within the best of its ability, given the limitations described earlier. This is instructive as, assuming the TIEGCM model can replicate the propagation of these tides to ~150 km altitude, the model can be used to compute the $\Sigma O/N_2$ perturbation that would be expected given the tides present on these days and to explore differences between the modeled and observed O/N_2. Figure 8 shows the wavenumber-4 pattern in the neutral winds at 150 km altitude and the $\Sigma O/N_2$ from TIEGCM as a function of local time. The model results come from an average over DOY 75 – 95 when ICON sees the strongest $\Sigma O/N_2$ signature. The results are shown at 25 – 35° latitude to match the ICON wind observations in Figure 6 and ICON $\Sigma O/N_2$ in Figure 7. In the TIEGCM results, an eastward motion of the perturbation in all parameters with a phase speed matching that of DE3 is clearly evident across all daytime LT. The amplitude of the horizontal wind perturbations match those observed by ICON well, confirming that the model is reproducing some of the aspects of the propagation of a dominant DE3 tide up to 150 km altitude. Recalling the limitations of the lower boundary forcing described in Section 2.5, one visible difference between Figure 6 and Figure 8 is a phase shift in both the zonal and meridional winds is seen between those observed and those simulated, which may imply that the vertical wavelength of the tide is different in the model compared to that observed. Nonetheless, the overall similarity in the wind magnitudes suggests that we can use the results of the TIEGCM model to provide an indication of what impact the DE3 and SE2 tides may have on $\Sigma O/N_2$.

The simulated vertical winds, which are not observed, also show a similar eastward motion that very closely matches that expected for DE3. The $\Sigma O/N_2$ likewise shows an eastward propagation that is similar to that in the winds. The amplitude of the signature shows some variation with LT, as may be expected given the presence of the SE2 perturbation, such that the amplitude seen before ~9 LT is the largest, although the amplitude is also large between ~12 – 15 LT. The maximum amplitude seen in $\Sigma O/N_2$ at any time is ~2% which is a factor of 1.5 – 2 times smaller than the pre-noon values observed by ICON. As this is primarily produced by the vertical wind perturbation, it can be assumed that the vertical wind perturbation in the TIEGCM model is smaller than that in the atmosphere, although no direct observations exist to confirm this. Such a mismatch in the vertical wind would also be consistent with a mismatch in the vertical wavelength of the tide in the model compared to the atmosphere. The strength of the $\Sigma O/N_2$ signature in the 12 – 15 LT range suggests that ICON may be expected to see a clear signature at this time (while the signature is weaker in the afternoon than the morning, a clear signature at this amplitude should be easily detected in the observations as discussed above). This would indicate that the presence of an O^+ radiative recombination signal is the most likely cause of the changes observed in Figure 7 after ~13 LT.

To investigate the possibility of O^+ radiative recombination contaminating the wavenumber-4 $\Sigma O/N_2$ perturbations seen with ICON, we make use of the ICON EUV O^+ observations. Any potential O^+ radiative recombination can be estimated from examining both the column O^+ and NmF2 values determined from these data. Figure 9 shows the wavenumber-4 perturbation in NmF2 and O^+ as functions of longitude and local time. Here only the descending portion data are shown, which provides observations at an overlapping DOY range as the clearest signal in the $\Sigma O/N_2$ observations (the ascending node data sample this region from DOY 62 – 76, with the afternoon data all occurring before DOY 68 and thus do not provide a good source of comparison to the $\Sigma O/N_2$ observations). It is worth noting here that in the range that is used in Figure 9, the average uncertainty per sample is 16.7%. For the descending node, an average of 240 data points per day are used in the fit, yielding an uncertainty in the wavenumber-4 fit of around 2.2%. In both parameters from the EUV instrument, a significant wavenumber-4 signature is seen after ~13 LT, and only a much weaker signature is seen prior to this time. From ~13 – 16.9 LT there is some evidence of an eastward motion in these perturbations, but over such a short range of LT the rate of these is difficult to determine. Nonetheless, these data suggest that the wavenumber-4 O^+ radiative recombination signal would move eastwards with increasing local time and have become increasingly significant after ~13 LT. If the O^+ radiative recombination signal is not in phase with the $\Sigma O/N_2$ signature, this could therefore account for the inconsistent wavenumber-4 signature seen in Figure 7 after ~12 LT.

Shepherd et al., (2011) reported a wavenumber-4 variation in the brightness of the $O(^1S)$ 557.7 nm airglow near 250 km altitude. The ICON MIGHTI instrument is able to measure the brightness of this emission at 150 km altitude, close to the photoelectron peak and the neutral winds as shown in Figure 6. At this altitude, the brightness of this emission is believed to be produced mainly by $N_2(A^3\Sigma_u^+) + O$, where the excited N_2 is the minor species and is produced by photoelectron impact on N_2 (see Zhang and Shepherd, 2005 and references therein). This means that its variation in brightness may be expected to be in antiphase with the O/N_2 variations seen in Figure 7 and Figure 8. Figure 10 shows the observed wavenumber-4 perturbation in the 557.7 nm airglow observed with the ‘forward’ looking MIGHTI field of view (MIGHTI-A). Data are taken over DOY 75 – 100 to provide both overlap when the clear signature is seen in Figure 7 and provide sufficient LT coverage at the latitude range of these $\Sigma O/N_2$ observations. Once again, a clear eastward moving signature is seen throughout all daytime hours. As in Figure 6 and Figure 8, a variation in the amplitude of the signature is seen with LT and the eastward motion does not perfectly match that of DE3, suggesting that SE2 is present as well with some magnitude. The perturbation is also seen to be in near antiphase with the $\Sigma O/N_2$ observations in Figure 7 and model results in Figure 8. This provides confidence that the N_2 densities in the model are varying in a manner consistent with the atmosphere at this time, and implies that the O densities should do likewise, as both respond to the same vertical wind perturbations.

5. Conclusions

A survey of six months of ICON FUV sub-limb observations and retrieved $\Sigma O/N_2$ from 2020 is presented. From these we see variations in both the brightness of the airglow and

$\Sigma O/N_2$ that exhibit the expected SZA, latitudinal and seasonal variations. The uncertainties in the retrieved $\Sigma O/N_2$ increase slightly with SZA as may be expected given the variation in the photoelectron production altitudes with SZA. Uncertainties on single 12 second data points generally fall in the 5 – 10 % range except at large SZA. A comparison of the retrieved $\Sigma O/N_2$ and those predicted using NRL-MSISE00 show a consistent bias such that the ICON values are around 0.84 times the MSIS values, which is in good agreement with an analysis of TIMED-GUVI observations at solar minimum reported by Meier et al., [2015].

An examination of the impact of non-migrating tides on the $\Sigma O/N_2$ is presented. This is done by focusing on a time period in early 2020 when ICON clearly sees the DE3 non-migrating tide in the winds and temperatures near the base of the thermosphere, and the winds at 150 km altitude. At this time, some SE2 is also observed, contributing to the wavenumber-4 signature in fixed local time in addition to DE3. Following prior studies, we examine the observations away from the equator in an attempt to minimize the effect of O^+ radiative recombination and focus on a region from 25 – 35° north where we have data from all instruments on nearly the same DOY. Using the tides observed in the MLT region as a lower boundary condition, we also perform a simulation with the TIEGCM model to provide context for the ICON observations. From these we see a wavenumber-4 perturbation in the retrieved $\Sigma O/N_2$ that is small (below ~5% of the zonal mean value). During the morning, the signal is comparatively clear and can be seen to move eastwards with increasing local time, but this pattern breaks down in the afternoon. Three reasons for this morning to afternoon change are considered: a change in the strength of the signature with local time; a change in the strength of the signature with DOY; and the effect of an overlapping wavenumber-4 signature in the O^+ radiative recombination that becomes stronger in the afternoon. From an examination of the ICON observations of $\Sigma O/N_2$ and other parameters, the first two of these are considered to be less likely than the impact of contamination of the SW dayglow signal by radiative recombination, in agreement with Kil and Paxton, [2011] and Kil et al., [2013]. ICON wind observations clearly shown the presence of a wavenumber-4 pattern generated from DE3 and SE2 is present at the altitude of the photoelectron emissions, the source of the $\Sigma O/N_2$ observations. While these vary with LT, they are clear throughout the daytime. During the same interval, the TIEGCM model shows a clear $\Sigma O/N_2$ perturbation should be clear throughout the day. The ICON O^+ observations in the afternoon (~13 – 16.9 LT) show some evidence of an eastward motion of a wavenumber-4 structure, but over such a short range of LT the rate of these is difficult to determine. The structure seen in the O^+ observations do not appear to be in phase with the $\Sigma O/N_2$ perturbation. Taken together, its seems reasonable to infer that there is some tidal pattern in the $\Sigma O/N_2$ observations (along with other variability), which is made unclear when there is significant O^+ radiative recombination in the SW dayglow signature used to determine $\Sigma O/N_2$. Using data near 15:00 LT, Kil et al., [2013] estimated that the $\Sigma O/N_2$ retrieved was perturbed by ~5 – 10 % by O^+ radiative recombination. This value is larger than tidal impact on $\Sigma O/N_2$ seen here, and is consistent with our finding of the contamination of the dayglow signature during the afternoon. These conclusions underline the limitation of using the retrieved $\Sigma O/N_2$ values retrieved from sub-limb FUV airglow to determine small wave-induced perturbations. But the analysis does demonstrate that the observations can provide a by-eye estimation of the

tidal modulation of the $\Sigma O/N_2$ in the morning thermosphere, at least at latitudes away from the peak of the equatorial ionospheric arcs.

The observed variation in $\Sigma O/N_2$ is generally larger than that in the TIEGCM model at the same time, which suggests the model is underestimating the wavenumber-4 component of the vertical wind that creates the $\Sigma O/N_2$ perturbation. While the TIEGCM model replicates the observed horizontal wind amplitudes near 150 km well, the phase of the wavenumber-4 signature does not agree with that observed. If the model produces a DE3 tide with the incorrect vertical wavelength, that would also be consistent with both the incorrect horizontal wind phase and vertical wind. This analysis demonstrates the utility of the combined ICON datasets, especially when used in conjunction with first-principles models.

Acknowledgements

This analysis used version 04 of the Level 2.4 ICON-FUV data, version 04 of the Level 2.2 ICON-MIGHTI data, version 02 of the Level 2.6 ICON-EUV data and version 01 of the Level 4.1 HME data which are available from the ICON website (https://icon.ssl.berkeley.edu/Data) and NASA's Space Physics Data Facility (https://cdaweb.gsfc.nasa.gov/pub/data/icon/). The TIEGCM winds and $\Sigma O/N_2$ are available at https://doi.org/10.7294/14495640. ICON is supported by NASA's Explorers Program through contracts NNG12FA45C and NNG12FA42I. The NRLMSISE-00 model is available from NASA's Community Coordinated Modeling Center (https://ccmc.gsfc.nasa.gov/pub/modelweb/). RRM acknowledges support from ICON via NASA's Explorers Program and the US Civil Service Retirement System.

References

Cui J, Yelle RV, Li T, Snowden DS, and Müller-Wodarg ICF (2014), Density waves in Titan's upper atmosphere, J. Geophys. Res. Space Physics, 119, 490–518, doi:10.1002/2013JA019113.

Cullens C, Immel TJ, Triplett CC, Wu Y-J, England SL, Forbes JM; Liu G (2020). Sensitivity Study for ICON Tidal Analysis. Progress in Earth and Planetary Science, PEPS-D-19-00045R2. Accepted, 04/20/20.

Dudis JJ, and Reber CA (1976), Compositional effects in thermospheric gravity waves, Geophys. Res. Lett, 3, 727–730, doi:10.1029/GL003i012p00727.

Emmert JT, Drob DP, Picone JM, Siskind DE, Jones M, Mlynczak MG, et al. (2020). NRLMSIS 2.0: A whole-atmosphere empirical model of temperature and neutral species densities. Journal Geophysical Research, e2020EA001321. 10.1029/2020EA001321

England SL, et al. (2016), Simultaneous observations of atmospheric tides from combined in situ and remote observations at Mars from the MAVEN spacecraft, J. Geophys. Res. Planets, 121, doi:10.1002/2016JE004997.

England SL, Immel TJ, Huba JD, Hagan ME, Maute A, DeMajistre R, Modeling of multiple effects of atmospheric tides on the ionosphere: an examination of possible coupling mechanisms responsible for the longitudinal structure of the equatorial ionosphere. J. Geophys. Res 115, 05308 (2010). doi:10.1029/2009JA014894

Englert CR, Harlander JM, Brown CM, Marr KD, Miller IJ, Stump JE, Hancock J, Peterson JQ, Kumler J, Morrow WH, Mooney TA, Ellis S, Mende SB, Harris SE, Stevens MH, Makela JJ, Harding BJ, and Immel TJ, 2017. Michelson Interferometer for Global High-resolution Thermospheric Imaging (MIGHTI): instrument design and calibration. Space Science Reviews, 212(1-2), pp.553–584. DOI: 10.1007/s11214-017-0358-4 [PubMed: 30008488]

Evans JS, Strickland DJ, Huffman RE and Eastes RW (1995), Satellite remote sensing of thermospheric O/N2 and solar EUV, 2. Data Analysis, J. Geophys. Res, 100, 12,217–12,226.

Forbes JM, Russell J, Miyahara S, Zhang X, Palo S, Mlynczak M, Mertens CJ, and Hagan ME (2006), Troposphere-thermosphere tidal coupling as measured by the SABER instrument on TIMED during July – September 2002, J. Geophys. Res, 111, A10S06, doi:10.1029/2005JA011492.

Forbes JM, Zhang X, Hagan ME, England SL, Liu G, Gasperini F, (2017). On the specification of upward-propagating tides for ICON science investigations. Space Science Reviews 212: 697. https://doi.org/150.1007/s11214-017-0401-5 [PubMed: 30093735]

Goncharenko LP, Chau JL, Liu H-L, Coster AJ, Unexpected connections between the stratosphere and ionosphere. Geophys. Res. Lett 37, 10101 (2010). doi:10.1029/2010GL043125

Harding BJ, Makela JJ, Englert CR, Marr KD, Harlander JM, England SL, and Immel TJ, (2017). The MIGHTI wind retrieval algorithm: description and verification. Space Science Reviews, 212: 585. 10.1007/s11214-017-0359-3 [PubMed: 30034033]

Hedin AE, Reber CA, Newton GP, Spencer NW, Brinton HC, Mayr HG, & Potter WE (1977). A global thermospheric model based on mass spectrometer and incoherent scatter data MSIS, 2. Composition. Journal of Geophysical Research, 82(16), 2148–2156. 10.1029/JA082i016p02148

Immel TJ, Sagawa E, England SL, Henderson SB, Hagan ME, Mende SB, Frey HU, Swenson CM, Paxton LJ, The control of equatorial ionospheric morphology by atmospheric tides. Geophys. Res. Lett 33, 15108 (2006). doi:10.1029/2006GL026161

Immel TJ, England SL, Mende SB et al. , (2018). The Ionospheric Connection Explorer Mission: Mission Goals and Design, Space Science Reviews, 214: 13. 10.1007/s11214-017-0449-2 [PubMed: 33758433]

Jones M Jr., Emmert JT, Drob DP, Picone JM, & Meier RR (2018). Origins of the thermosphere-ionosphere semiannual oscillation: Reformulating the “thermospheric spoon” mechanism. Journal of Geophysical Research: Space Physics, 123, 931–954. 10.1002/2017JA024861

Kil H, Lee WK, Shim J, Paxton LJ, and Zhang Y (2013), The effect of the 135.6nm emission originated from the ionosphere on the TIMED/GUVI O/N_2 ratio, J. Geophys. Res. Space Physics, 118, 859–865, doi:10.1029/2012JA018112.

Kil H, and Paxton LJ (2011), The origin of the nonmigrating tidal structure in the column number density ratio of atomic oxygen to molecular nitrogen, Geophys. Res. Lett, 38, L19108, doi:10.1029/2011GL049432.

Maute A, 2017. Thermosphere-Ionosphere-Electrodynamics General Circulation Model for the Ionospheric Connection Explorer: TIEGCM-ICON. Space Science Reviews, 212(1-2), pp.523–551. DOI: 10.1007/s11214-017-0330-3 [PubMed: 30026634]

Meier RR, et al. (2015) Remote Sensing of Earth’s Limb by TIMED/GUVI: Retrieval of thermospheric composition and temperature, Earth and Space Science, 2, 1–37, doi: 10.1002/2014EA000035.

Meier RR (2021). The thermospheric column O/N2 ratio. Journal of Geophysical Research: Space Physics, 126, e2020JA029059. 10.1029/2020JA029059

Mende SB, Frey HU, Rider K, Chou C, Harris SE, Siegmund OHW, England SL, Wilkins CW, Craig WW, Turin P, Darling N, Immel TJ, Loicq J, Blain P, Syrstadt E, Thompson B, Burt R, Champagne J, Sevilla P, Ellis S (2017), The far ultra-violet imager on the ICON mission. Space Sci. Rev 10.1007/s11214-ß017-0386-0

Nicholas AC, Craven JD, and Frank LA (1997), A survey of large-scale variations in thermospheric oxygen column density with magnetic activity as inferred from observations of the FUV dayglow, J. Geophys. Res, 102(A3), 4493–4510, doi:10.1029/96JA03464.

Oberheide J, and Forbes JM (2008), Tidal propagation of deep tropical cloud signatures into the thermosphere from TIMED observations, Geophys. Res. Lett, 35, L04816, doi:10.1029/2007GL032397.

Oberheide J, Forbes JM, Zhang X, Bruinsma SL (2011) Climatology of upward propagating diurnal and semidiurnal tides in the thermosphere. J. Geophys. Res 116, A11306. doi: 10.1029/2011JA016784.

Oberheide J, Pedatella NM, Gan Q, Kumari K, Burns AG, & Eastes R (2020). Thermospheric composition O/N2 response to an altered meridional mean circulation during Sudden Stratospheric Warmings observed by GOLD. Geophysical Research Letters, 47, e2019GL086313. 10.1029/2019GL086313

Picone JM, Hedin AE, Drob DP, and Aikin AC, (2002) NRLMSISE-00 empirical model of the atmosphere: Statistical comparisons and scientific issues, J. Geophys. Res, 107(A12), 1468, doi:10.1029/2002JA009430

Sagawa E, Immel TJ, Frey HU, Mende SB, Longitudinal structure of the equatorial anomaly in the nighttime ionosphere observed by IMAGE/FUV. J. Geophys. Res 110, 11302 (2005)

Schunk RW, (1983) The terrestrial ionosphere, in Solar-Terrestrial Physics (Carovillano RL and Forbes JM, eds.), 609, Reidel Publ. Co., Dordrecht.

Shepherd GG (2011), Thermospheric observations of equatorial wavenumber 4 density perturbations from WINDII data, Geophys. Res. Lett, 38, L08801, doi:10.1029/2011GL046986.

Sirk MM, Korpela EJ, Ishikawa Y, Edelstein J, Wishnow EH, Smith C, McCauley J, McPhate JB, Curtis J, and Gibson SR, 2017. Design and performance of the ICON EUV spectrograph. Space Science Reviews, 212(1-2), pp.631–643. DOI: 10.1007/s11214-017-0384-2 [PubMed: 33688106]

Stephan AW, Finn SC, Cook TA, Geddes G, Chakrabarti S, & Budzien SA (2019). Imaging of the daytime ionospheric equatorial arcs with extreme and far ultraviolet airglow. Journal of Geophysical Research: Space Physics, 124. 10.1029/2019JA026624

Stephan AW, Korpela EJ, Sirk MM, England SL and Immel TJ, (2017). Daytime Ionosphere Retrieval Algorithm for the Ionospheric Connection Explorer (ICON). Space Science Reviews, 212(1-2), pp.645–654 DOI: 10.1007/s11214-017-0385-1 [PubMed: 30034035]

Stephan AW, Meier RR, England SL, Mende SB, Frey HU and Immel TJ, (2018). Daytime O/N_2 Retrieval Algorithm for the Ionospheric Connection Explorer (ICON). Space Science Reviews, DOI: 10.1007/s11214-018-0477-6

Stevens MH, Englert CR, Harlander JM, England SL, Marr KD, Brown CM, and Immel TJ, (2018). Retrieval of Lower Thermospheric Temperatures from O_2 A Band Emission The MIGHTI Experiment on ICON, Space Science Reviews, 214: 4. 10.1007/s11214-017-0434-9 [PubMed: 30166692]

Strickland DJ, Cox RJ, Meier RR, and Drob DP (1999), Global O/N2 derived from DE 1 FUV dayglow data: Technique and examples from two storm periods", J. Geophys. Res, vol. 104, no. A3, pp. 4251–4266, 1999. doi:10.1029/98JA02817.

Strickland DJ, Evans JS, and Paxton LJ (1995), Satellite remote sensing of thermospheric O/N_2 and solar EUV, 1, Theory, J. Geophys. Res, 100, 12,217.

Torr MR, Torr D. (1985). Ionization frequencies for solar cycle 21: revised. J Geophys Res: Space Phys 90 (A7): 6675–6678. 10.1029/JA090iA07p06675.

Zhang Y, Paxton LJ, Morrison D, Wolven B, Kil H, Meng C-I, Mende SB, and Immel TJ (2004), O/N2 changes during 1–4 October 2002 storms: IMAGE SI-13 and TIMED/GUVI observations, J. Geophys. Res, 109, A10308, doi:10.1029/2004JA010441.

Zhang SP, and Shepherd GG (2005), On the response of the $O(^1S)$ dayglow emission rate to the Sun's energy input: An empirical model deduced from WINDII/UARS global measurements, J. Geophys. Res, 110, A03304, doi:10.1029/2004JA010887.

Zhang Y, England S, and Paxton LJ (2010), Thermospheric composition variations due to nonmigrating tides and their effect on ionosphere, Geophys. Res. Lett, 37, L17103, doi:10.1029/2010GL044313.

Key points

1. An initial overview of the ICON FUV sub-limb observations and derived column O/N_2 ratios is presented
2. In the morning, away from the equatorial ionosphere, the impact of non-migrating tides on O/N_2 is shown clearly for the first time
3. Comparison of the tidal signature with the TIEGCM model highlights basic agreement, with possible discrepancy in tidal vertical wavelength

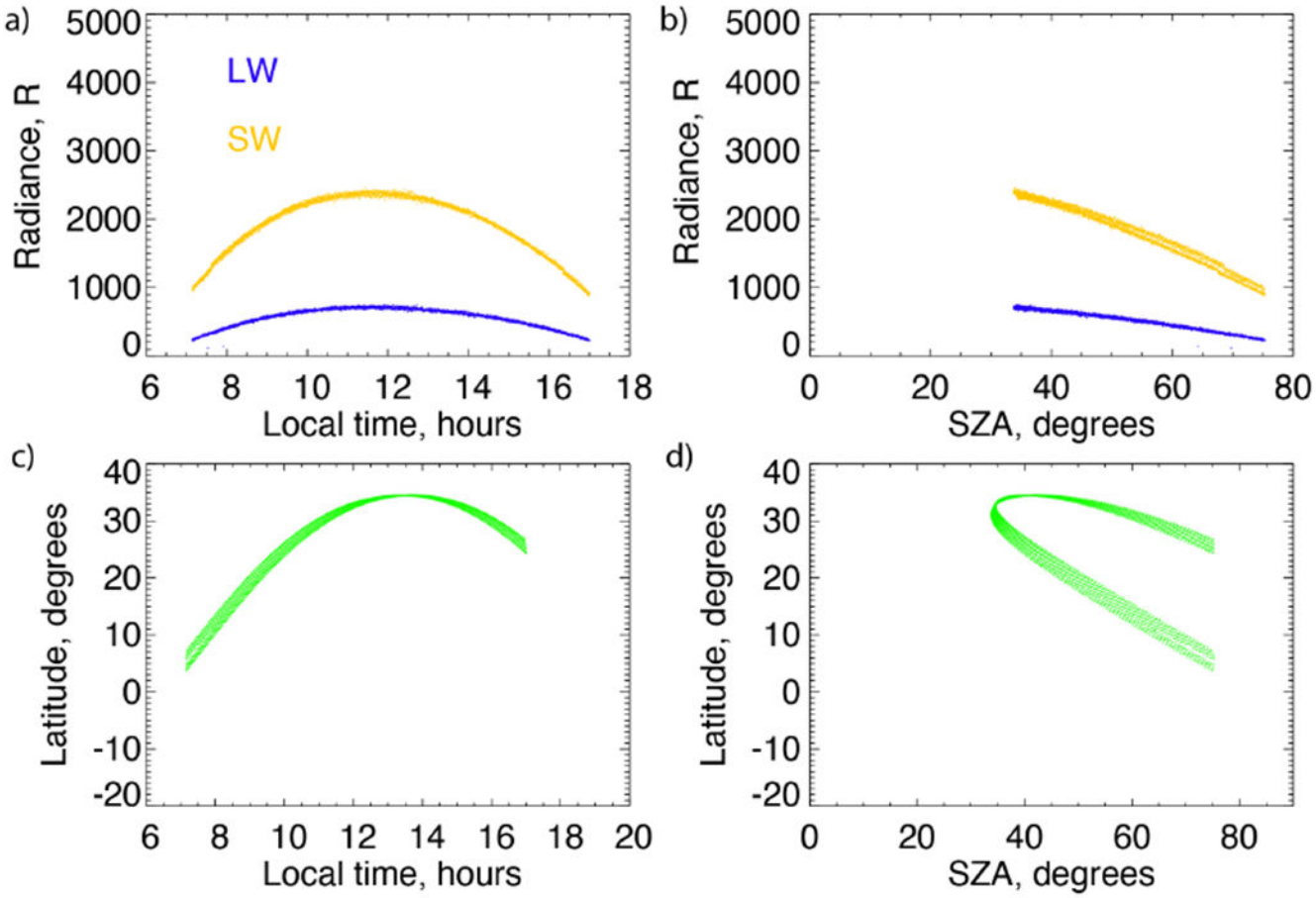

Figure 1.

Observed sub-limb FUV SW and LW airglow brightness for March 15, 2020. Panel a shows the brightness of the two airglow features as a function of local time. Panel b shows the brightness of the two airglow features as a function of solar zenith angle. In Panels a and b, the yellow points correspond to the SW airglow passband and the blue points correspond to the LW airglow passband. Panel c shows the location of the observed points, as a function of latitude and local time. Panel d shows the location of the observed points, as a function of latitude and solar zenith angle.

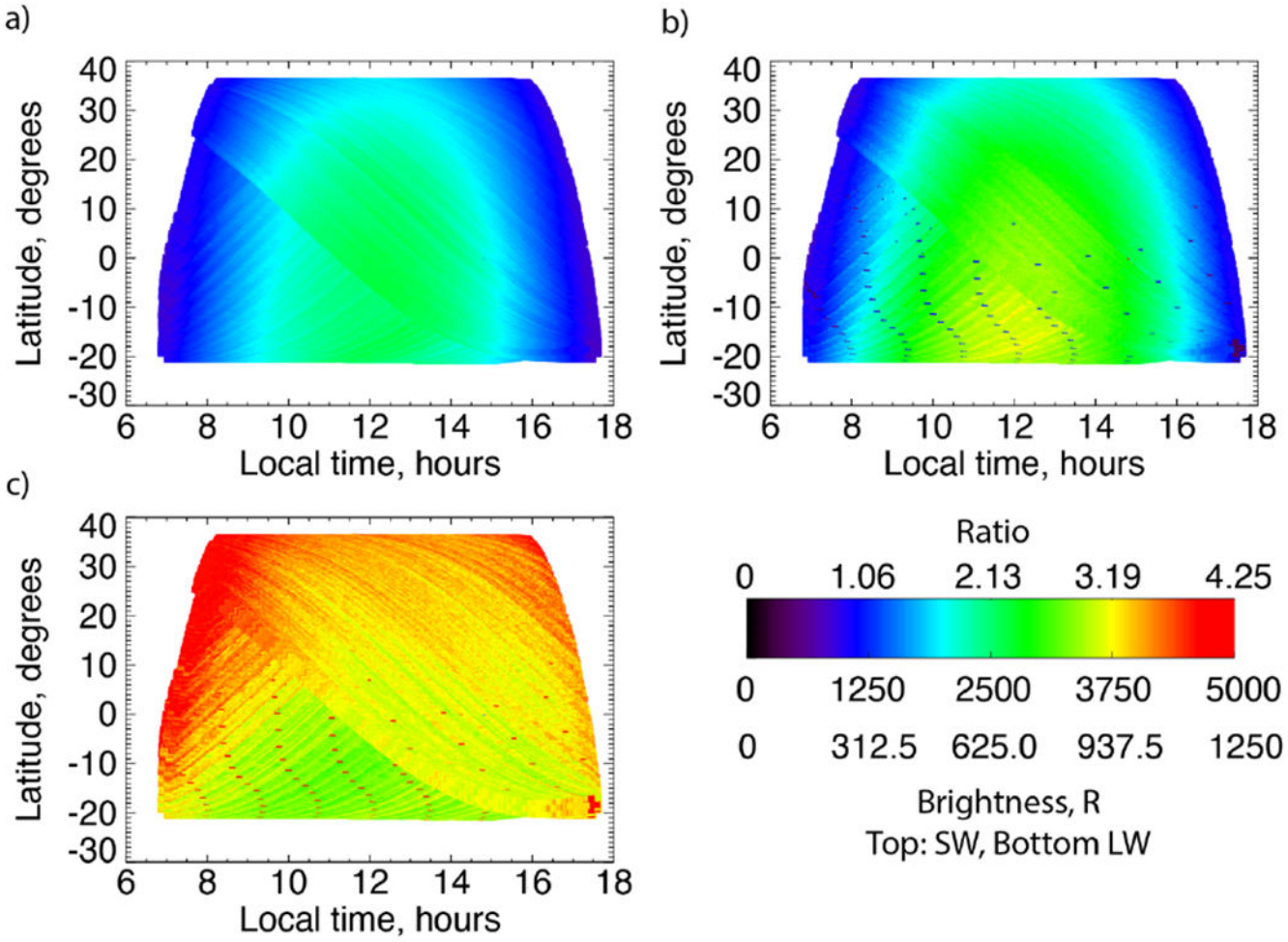

Figure 2.

Brightness of the SW and LW airglow and their ratio for days 1 – 45 of 2020. Panel a shows the brightness of the SW airglow as a function of latitude and local time. Panel b shows the brightness of the LW airglow as a function of latitude and local time. Panel c shows the ratio of the brightness of the SW to the brightness of the LW airglow as a function of latitude and local time.

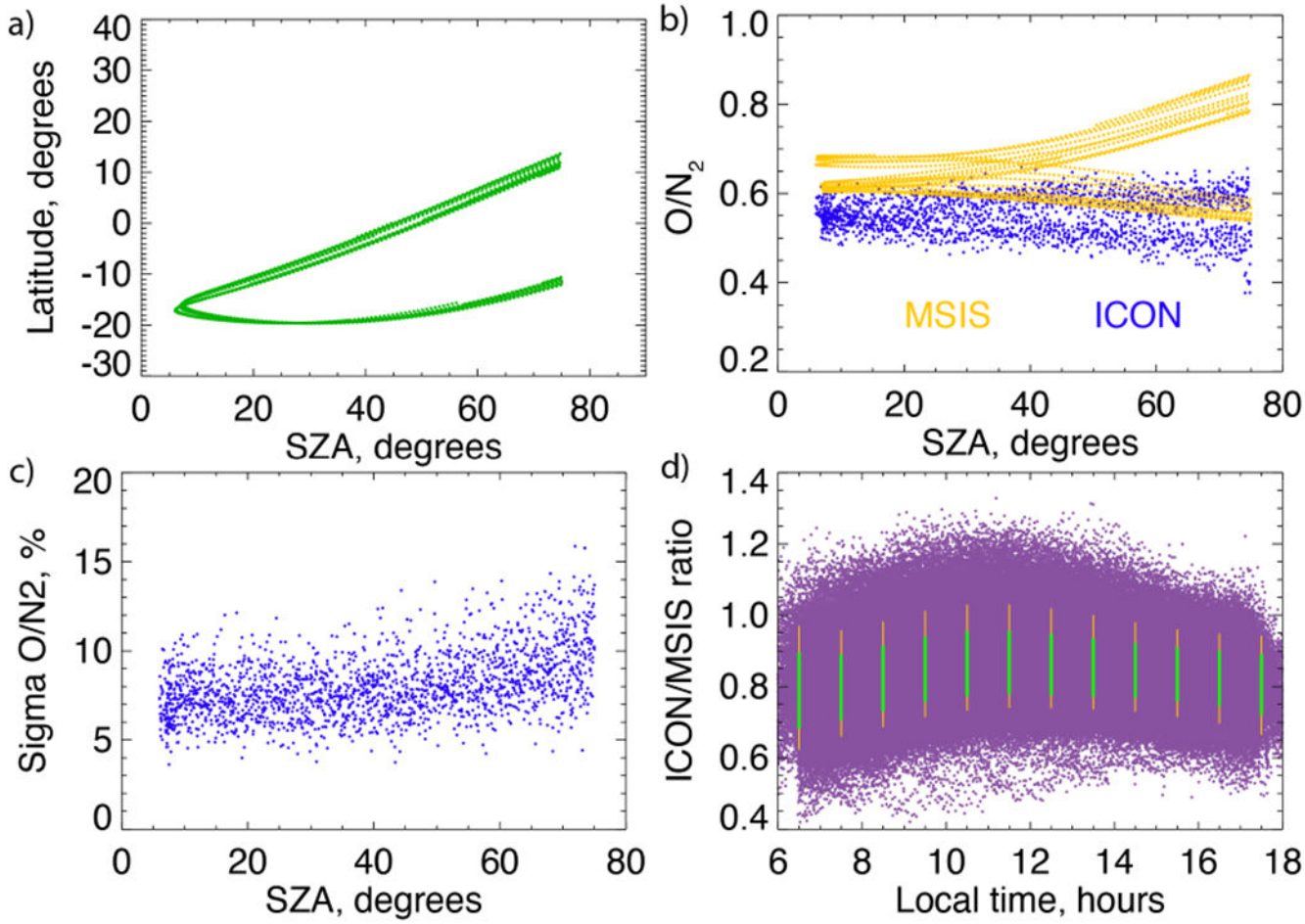

Figure 3.

Retrieved $\Sigma O/N_2$ compared to the MSIS model. Panel a shows the location of the observations on January 2, 2020 as a function of latitude and solar zenith angle. Panel b shows the retrieved $\Sigma O/N_2$ from ICON and the MSIS model for each point observed during January 2, 2020, as a function of solar zenith angle. Panel c shows the one standard deviation uncertainty in each of the retrieved $\Sigma O/N_2$ from ICON for each point observed during January 2, 2020, as a function of solar zenith angle. Panel d shows the ratio between the retrieved $\Sigma O/N_2$ from ICON and the MSIS model for each observation made during the first 6 months of 2020, as a function of local time. The purple dots represent the value for each observation. The green lines show the mean and standard deviation of these points at each 1-hour interval, and the orange line show the range from the 5^{th} to the 95^{th} percentile points at each 1-hour interval. The average ratio between ICON and MSIS is 0.84 and the average of the standard deviations is 0.089.

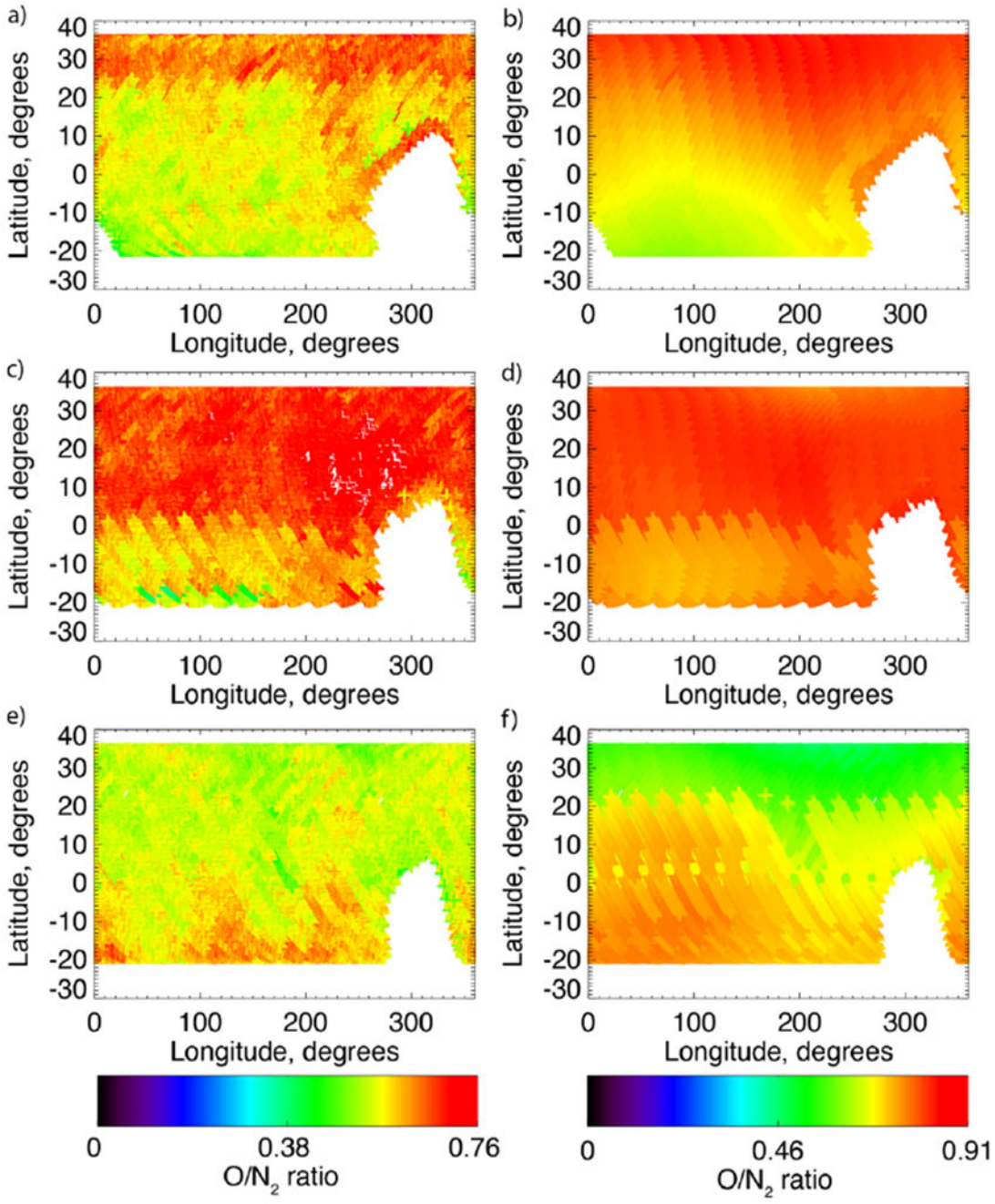

Figure 4.

geographic variation in the $\Sigma O/N_2$ from ICON and MSIS. Panels a, c and e show the ICON values and panels b, d, and f show the MSIS values. Panels a and b are for days 1 – 45, 2020. Panels c and d are for days 46 – 90, 2020. Panels e and f are for days 136 – 180, 2020. All values are from 11 – 13 hours local time. Note the different color scales used for the ICON and MSIS values, such that the variations with latitude and season are visible. Note that data are not available in the southern hemisphere near 300 degrees longitude as these

remote observation locations correspond to when the ICON spacecraft is within the South Atlantic Anomaly.

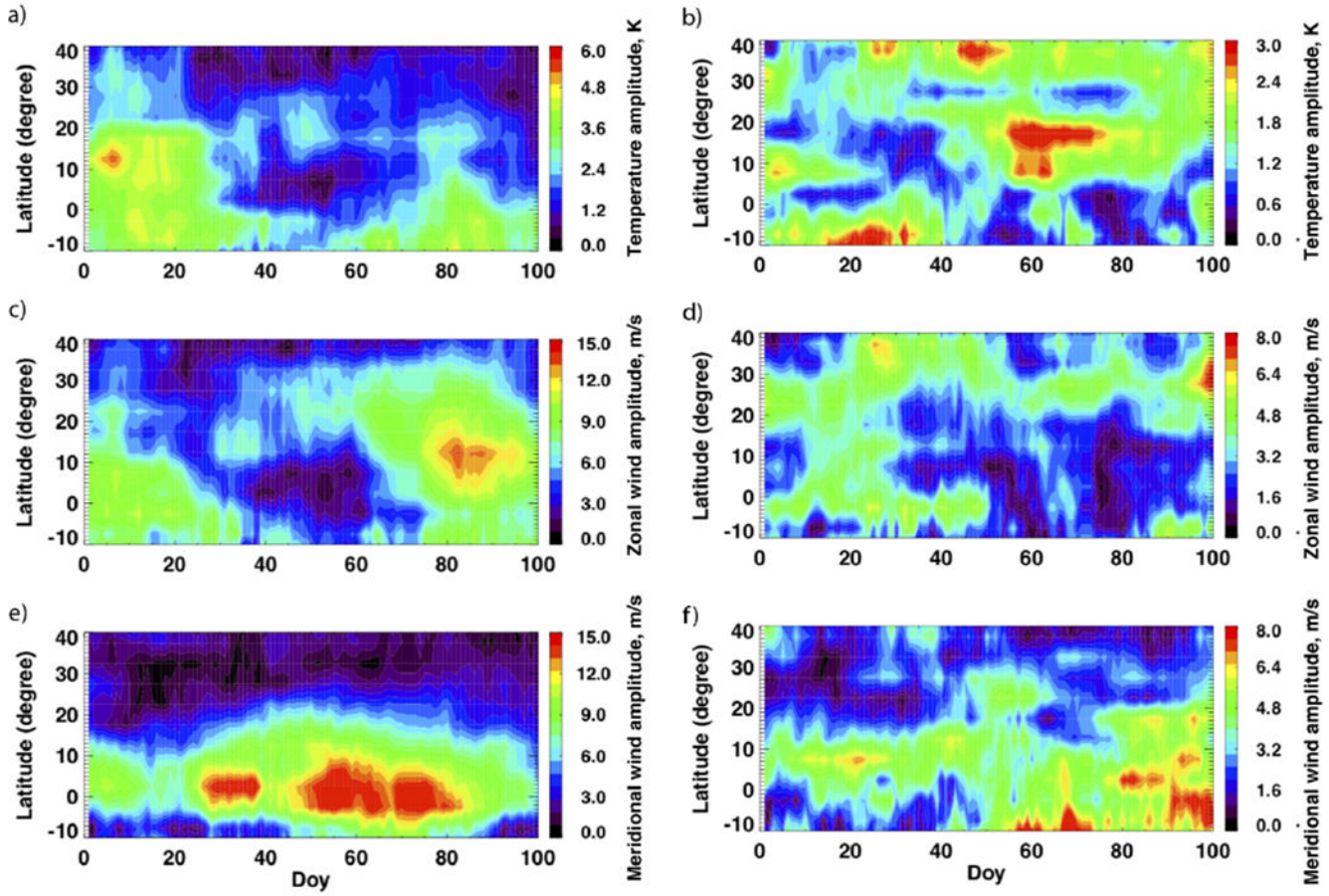

Figure 5.

Amplitude of the DE3 and SE2 non-migrating tides observed by MIGHTI at 97 km altitude during the first 100 days of 2020. Panels a, c and e correspond to the DE3 tide and panels b, d and f correspond to the SE2 tide. Panels a and b show the temperature amplitude, panels c and d show the zonal wind amplitude and panels e and f correspond to the meridional wind amplitude. All values are shown at 97 km altitude, corresponding to the lower boundary of the TIEGCM model. Note the different scales used in each panel.

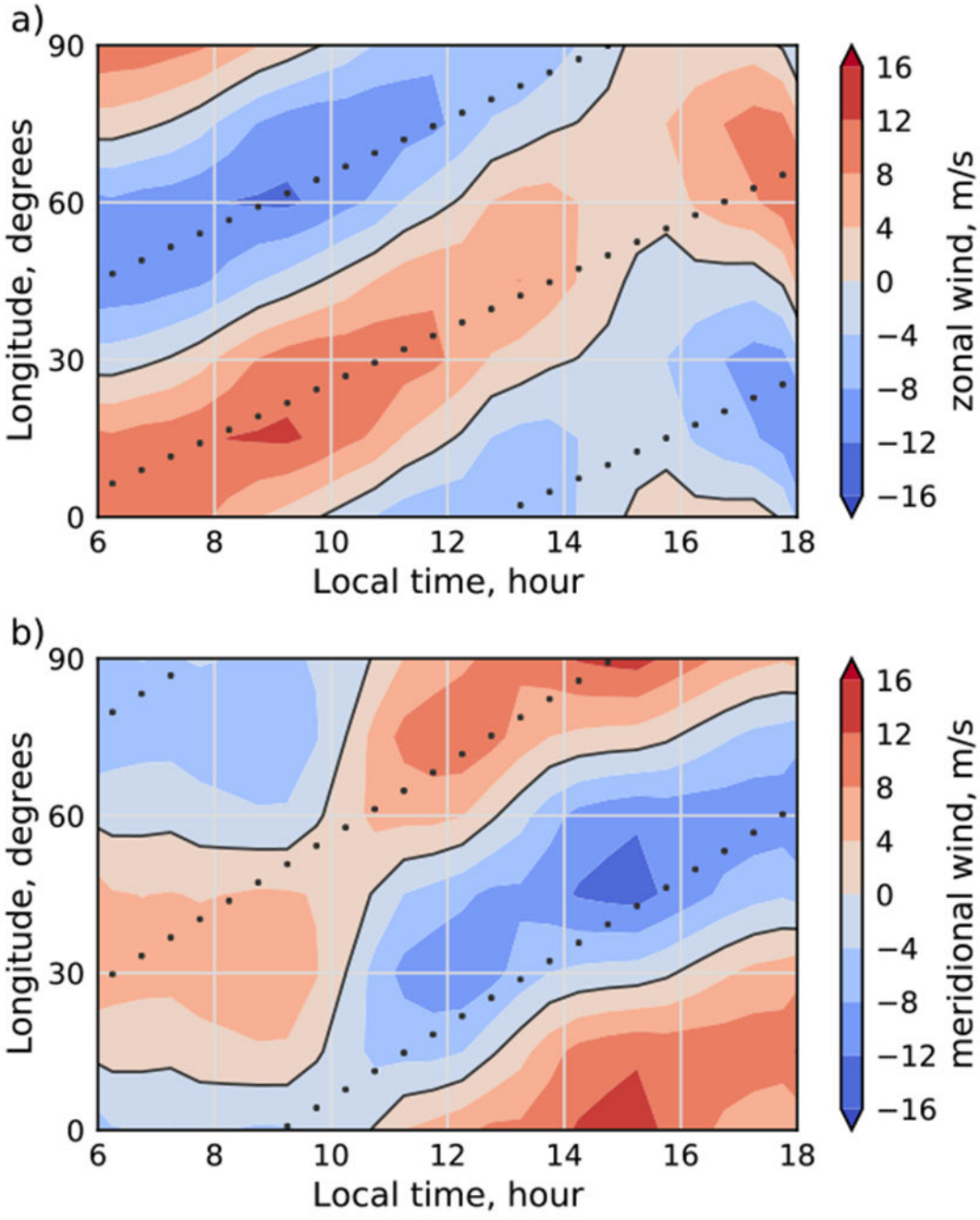

Figure 6.

Wavenumber-4 component of the horizontal winds observed by MIGHTI as functions of longitude and local time. Panel a shows the zonal wind perturbation and panel b shows the meridional wind perturbation. All data represent the wavenumber-4 fit to the data that are averaged over days 75 – 100, 2020, altitudes from 150 – 160 km altitude and 25 – 35° north. The best-fit linear trend in the zonal wind (meridional wind) of 5.12° (7.00°)/ hour is shown with the black dotted lines.

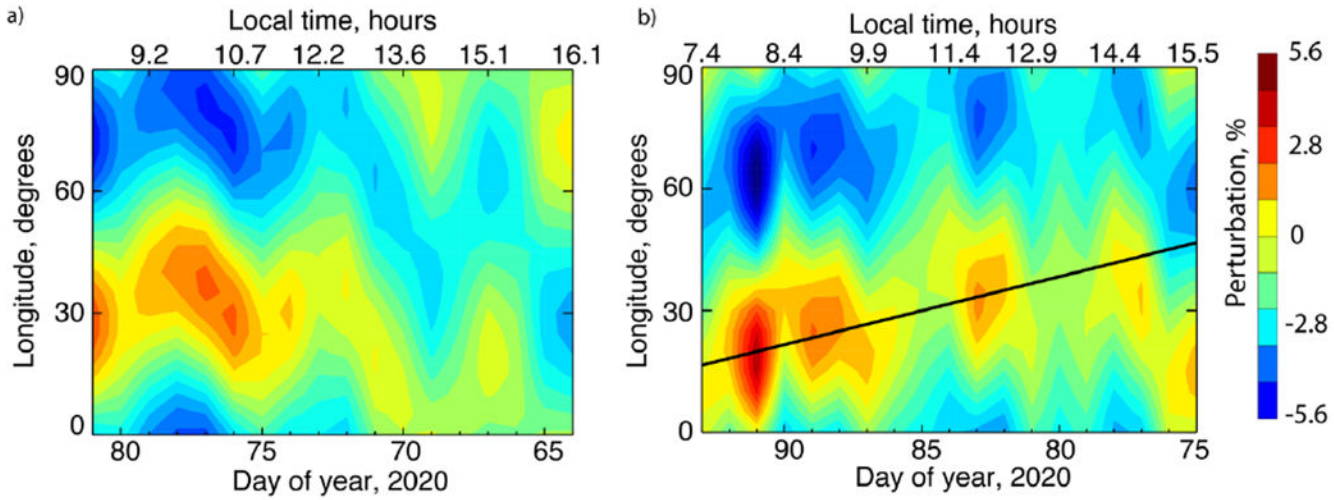

Figure 7.

Wavenumber-4 component of the perturbation in the $\Sigma O/N_2$ retrieved from the ICON observations as functions of day of year, local time and longitude. Panel a shows the data from the ascending portion of the orbit and panel b shows the data from the descending portion of the orbit. All data are averaged over 25 – 35° north. The $\Sigma O/N_2$ perturbation is determined relative to the mean value at each day of year (corresponding to a single local time). The solid line shown in panel b indicates the phase shift with local time expected for the DE3 tide and is included as a visual guide.

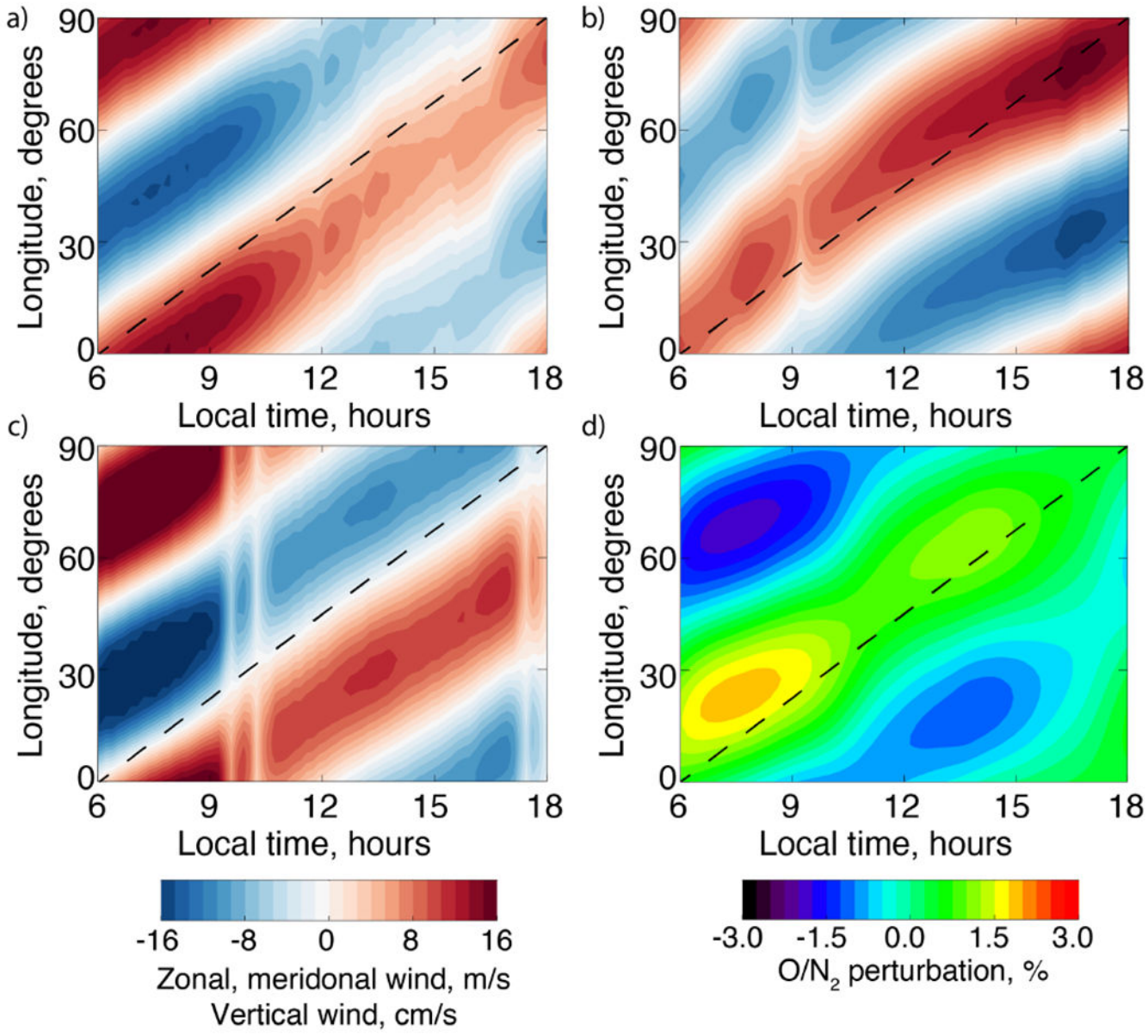

Figure 8.

Wavenumber-4 perturbation in the neutral winds and $\Sigma O/N_2$ ratios from the TIEGCM model as functions of local time and longitude. Values are averaged over 25 to 35° north and over days 75 – 95 of 2020. Panels a – c show the perturbation in the zonal, meridional and vertical wind respectively. The horizontal winds are shown in m/s and the vertical wind is shown in cm/s. Panel d shows the perturbation to the $\Sigma O/N_2$ and is expressed as a percentage of the zonal mean value at each local time. The dashed black line shows a phase shift of 3.75° / hour as would be expected from a DE3 tide.

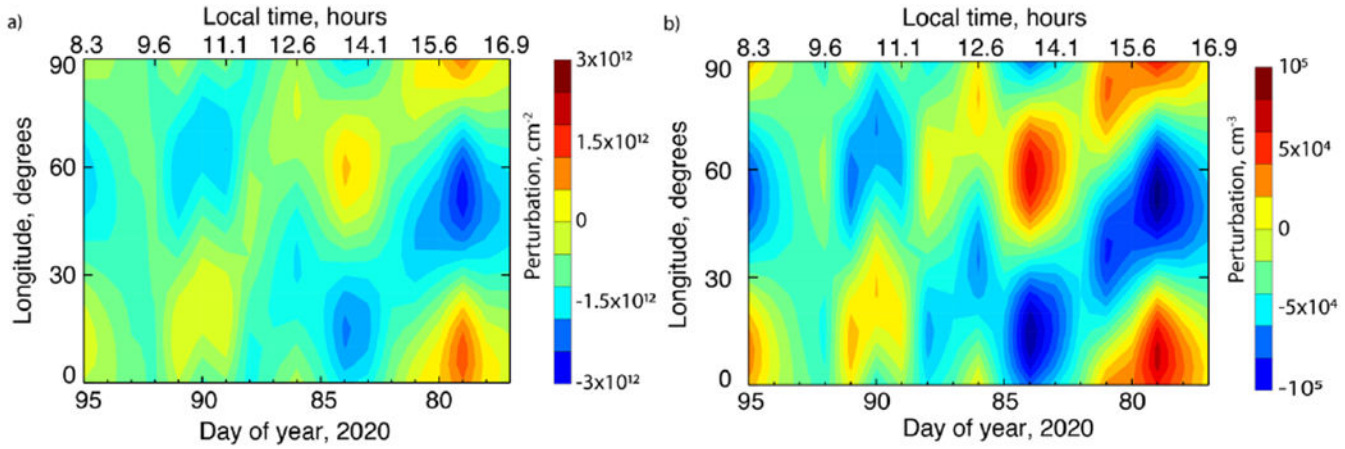

Figure 9.

Wavenumber-4 component of the pertrubation in ionospheric nmF2 and column O^+ abundance retrieved from ICON EUV observations as functions of day of year and longitude. Panel a shows the perturbation in the total column O^+ and panel b shows the perturbation in the NmF2 value. All data are from the descending portion of the orbit and are averaged over 25 – 35° north.

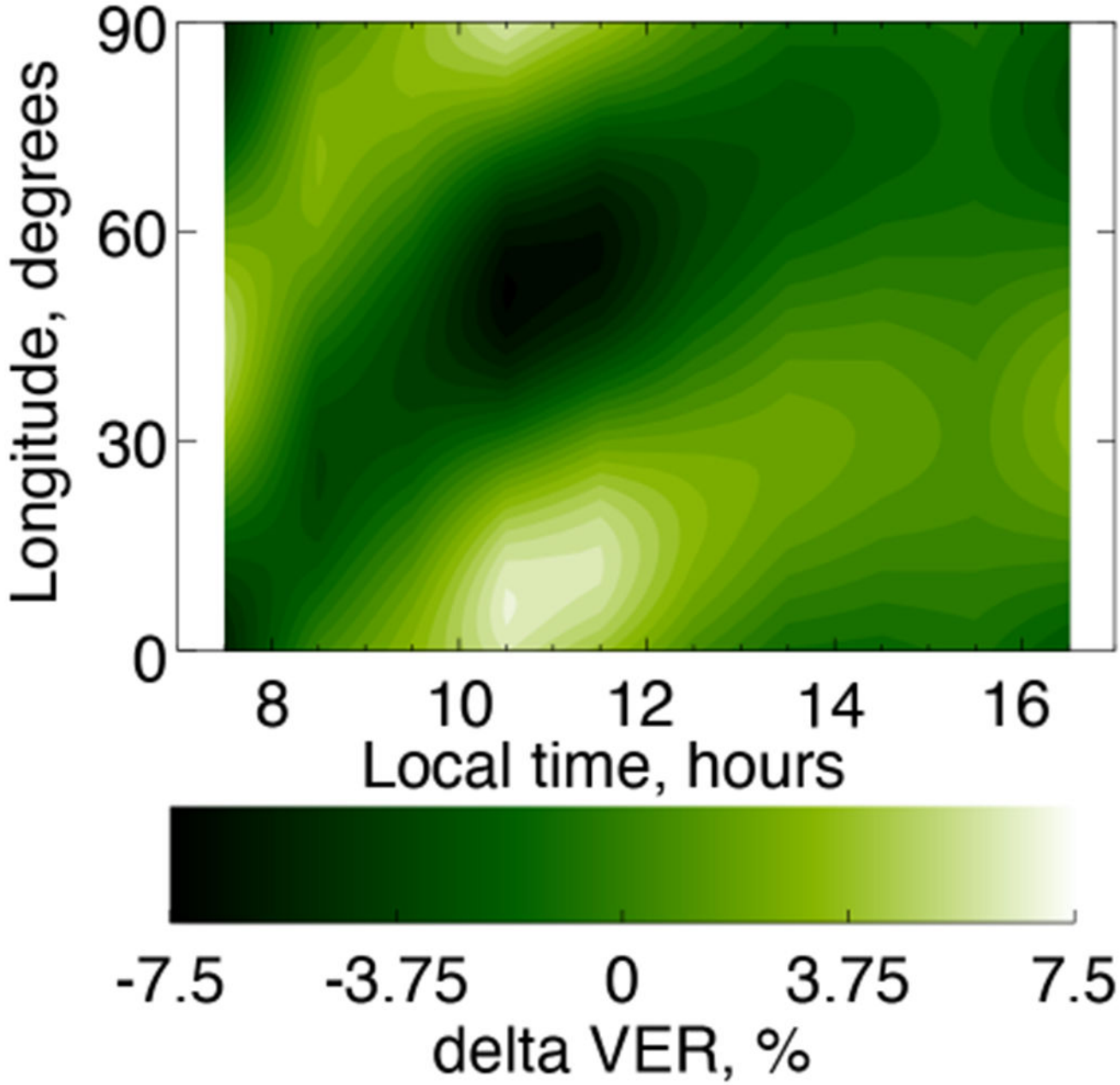

Figure 10.

Wavenumber-4 perturbation of the 557.7 nm airglow observed by MIGHTI Channel A as a function of local time and longitude. All data are averaged over days 75 – 100, 2020, tangent altitudes from 150 – 160 km altitude and 25 – 35° north. All values are expressed as a percent of the zonal mean value.